Appendix to "Numerical simulations of boundary-layer bypass transition due to high-amplitude free- stream turbulence"

By V. Ovchinnikov, M. M. Choudhari & U. Piomelli

Journal of Fluid Mechanics, vol. 613 (2008), pp. 135–169

A.1. Evolution of the integral length scale of the FST

In figure 20 we show the evolution of the FST integral length scale L_{33} computed by integrating the spanwise autocorrelation function of the spanwise velocity component. In the figure we also compare our data to power law fits of the form $y = C\,(x - x_0)^{1/2}$ (Roach 1987), assuming that L_{33} is an adequate approximation to L_{11}. It can be seen that in both cases SLS and T3B, L_{33} grows more slowly than the corresponding power law. One possible explanation is that the finite size of the computational domain prevents natural growth of free-stream eddies.

A.2. Reynolds stress profiles in curvilinear coordinates

In this section we compare the evolution of the Reynolds stresses along the curvilinear coordinate of the super-elliptical leading edge for the symmetry-line and full-domain cases. In figures 23a and 23c we compare mean velocity profiles for cases SLSs/f and T3Bs/f, respectively, and in figures 23b and 23d, Reynolds stresses. We use the notation $\langle\eta\eta\rangle$ and $\langle\xi\xi\rangle$ to denote Reynolds stress components tangent and perpendicular to the surface. Note that at the tip of the superellipse, $s = 0$, $\langle\eta\eta\rangle$ and $\langle\xi\xi\rangle$ correspond to $\langle vv\rangle$ and $\langle uu\rangle$, respectively, which denote Reynolds stress components in rectilinear coordinates. Away from the leading edge axis, $\langle\eta\eta\rangle$ and $\langle\xi\xi\rangle$ approach $\langle uu\rangle$ and $\langle vv\rangle$. The figures suggest that the differences in the evolution of the streamwise Reynolds stress $\langle uu\rangle$ downstream of the leading edge can be explained by different levels of the tangential Reynolds stress $\langle\eta\eta\rangle$ at the leading edge (where it corresponds to $\langle vv\rangle$). It is zero for cases SLSs and T3Bs because of the symmetry condition.

A.3. TKE budget

In this section we discuss the budget of the TKE across the transitional region. Figure 24 shows the development of the TKE budget corresponding

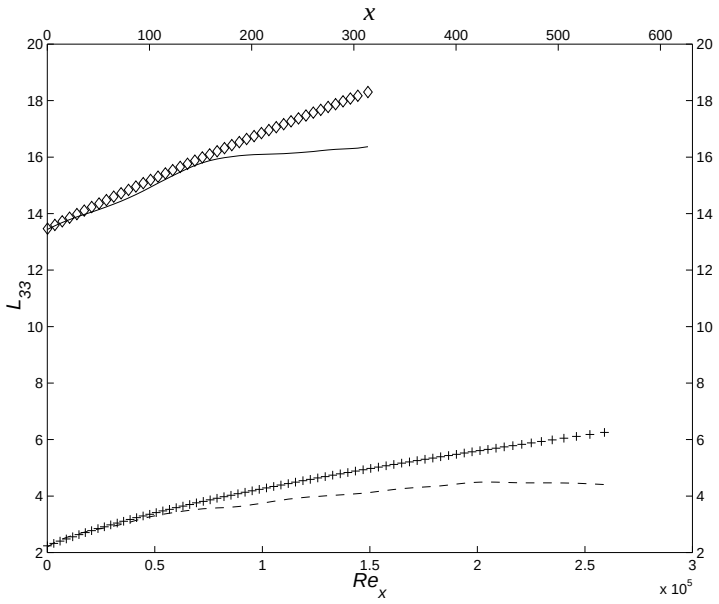

Figure 20: Evolution of the FST integral length scale L_{33} inside the boundary layer; —— T3B; - - - SLS; $\diamond$ Power law: $y = C\,(x - x_0)^{\alpha}$ with $\alpha = 0.5$ $x_0 = -370$, $C = 0.7$; +Power law: $y = C\,(x - x_0)^{\alpha}$ with $\alpha = 0.5$ $x_0 = -75$, $C = 0.26$;

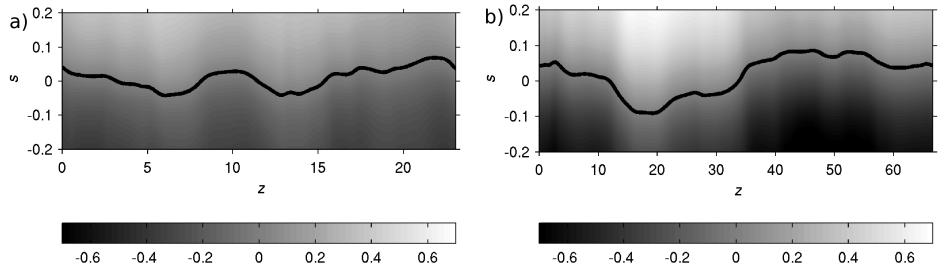

Figure 21: Instantaneous stagnation line and tangential velocity contours at n=0.03; (a) case SLSf; (b) case T3Bf; n denotes the wall-normal coordinate.

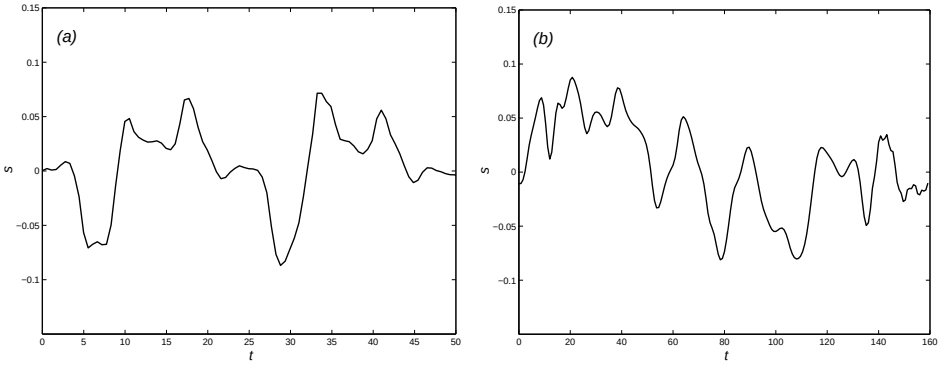

Figure 22: Evolution of the stagnation point in the middle of the domain. (a) case SLSf, $z = 11.5$; (b) case T3Bf, $z = 33$;

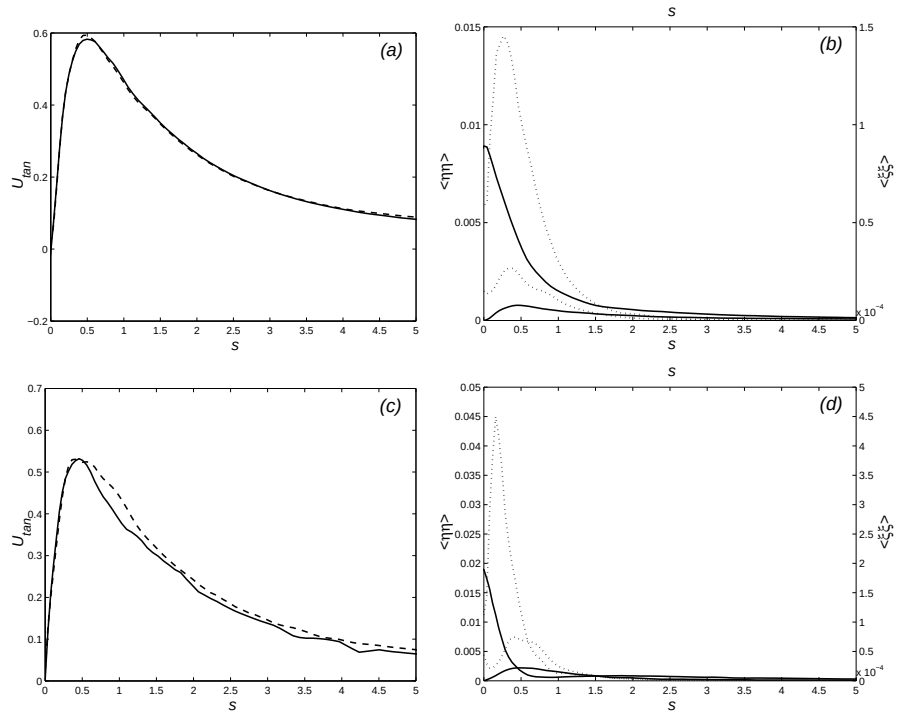

Figure 23: Wall-normal and streamwise Reynolds stress along the leading edge surface at $n \simeq 0.03$ where n is the wall-normal coordinate. (a) Tangential velocity; —— SLSs ; - - - SLSf (b) —— tangential Reynolds stress, $\langle \eta\eta \rangle$. ..... wall-normal Reynolds stress, $\langle \xi\xi \rangle$. For each Reynolds stress component, the upper curve corresponds to case SLSf, and the lower curve, to case SLSs. The left axis corresponds to $\langle \eta\eta \rangle$, and the right axis, to $\langle \xi\xi \rangle$. (c) same as (a) but for the T3B cases; (d) same as (b) but for the T3B cases.

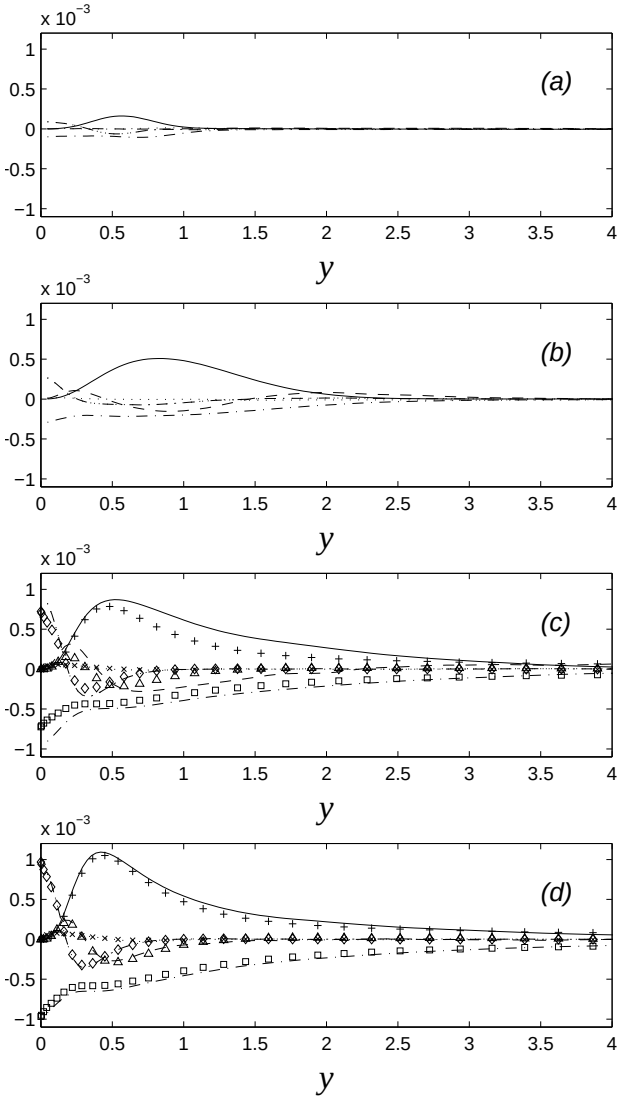

Figure 24: Budgets of the TKE at various locations; T3Bs case. All terms are normalized by U_∞ and R. (a) $x = 25, Re_x = 12,500, \delta_{99} = 1.12$; (b) $x = 100, Re_x = 50,000, \delta_{99} = 2.41$; (c) $x = 193, Re_x = 91,500, \delta_{99} = 4.36$; (d) $x = 260, Re_x = 123,250, \delta_{99} = 6.13$. Symbols: channel-flow DNS by Moser *et al.* 1999; lines: present simulation. +, ——— : production; □ , —·— Dissipation; △ , - - - Turbulent transport; × , ····· Pressure diffusion; ◇ , —··— Viscous diffusion.

to the T3Bs case. The terms are given by

$$\frac{\partial k}{\partial t} = -\langle U_i \rangle \frac{\partial k}{\partial x_j} - \frac{\partial \langle U_i \rangle}{\partial x_j} \langle u_i' u_j' \rangle - \nu \left\langle \frac{\partial u_i'}{\partial x_j} \frac{\partial u_i'}{\partial x_j} \right\rangle - \frac{1}{\rho} \frac{\partial \langle p' u_i' \rangle}{\partial x_i} + \nu \nabla^2 k - \frac{1}{2} \frac{\partial \langle u_j' u_i' u_i' \rangle}{\partial x_j}. \tag{1}$$

The quantities on the right side of (1), which is derived from the Reynolds-Averaged Navier-Stokes (RANS) equations, are referred to, respectively, as advection, production, dissipation, pressure work, viscous diffusion, and turbulent transport.

The sum of the computed terms in the budgets was very small throughout the computational domain, indicating good convergence. For example, in the fully-turbulent region, the maximum imbalance was 3% of the maximum production.

Our focus is on the T3B case but the differences from the other cases will be noted. The data are normalized by the free-stream velocity and the LE radius (both constant outer-coordinate scales), and thus are not in wall units. This choice was made in order to separate the effects of the mean flow evolution (which enters through the change in u_τ) from the evolution of the budget terms, which involve higher-order moments. The figure illustrates that the boundary layer TKE production maximum is initially near the middle of the laminar boundary layer. As the perturbed-laminar boundary grows, the peak in the production slowly moves farther away from the wall, consistent with the boundary-layer growth, up to the onset of transition at $x = 100$; beyond this location, it moves rapidly toward the wall. In the transitional and turbulent regions, the location of the production peak approximately coincides with the location of the maximum $u_{\rm rms}$. This maximum is due primarily to low-frequency modes of the streamwise velocity, as shown in the next section. At $x = 25$, ($Re_x \simeq 12,500$), the only active terms in the budget are the production, viscous diffusion, and viscous dissipation. The viscous terms balance each other at the wall, and together balance the production in the middle of the boundary layer. At $x = 100$, ($Re_x \simeq 50,000$) (plot *b*), the magnitudes of the budget terms are, on the average, 40% of their turbulent values at $x = 260$, ($Re_x = 123,250$). The viscous diffusion and dissipation have increased in magnitude near the wall, and the growing production is now balanced, in addition, by the turbulent transport and the advection (not shown for clarity of the plot). By $x = 193$, ($Re_x = 91,500$), the budget is nearly that of a turbulent near-wall flow. At this and at the final location, $x = 260$, ($Re_x = 123,250$), we have also plotted the turbulent channel data of Moser *et al.* (1999) obtained at $Re_\tau = 395$ for comparison (the use of channel rather than boundary layer data for comparison is justified because the near-wall behavior of the two flows is very similar). To

convert the channel data to outer coordinates, we used the local u_τ and ν from our simulation. The comparison in figure 24d shows that a turbulent equilibrium is fully established. An examination of the TKE budgets for cases SLSs & SLSf revealed a qualitatively similar development, except that the levels of production and the corresponding balancing terms were higher in the transitional region, in correlation with higher boundary-layer $u_{\rm rms}$ levels, as discussed in the next section. The perturbed laminar stage was characterized by a linear-like growth of the production peak, located approximately in the middle of the boundary layer. Across the breakdown stage, the production peak moved rapidly toward the wall, accompanied by a sharp increase in the magnitudes of the dissipation, diffusion and turbulent transport. In the fully-turbulent region, the budgets collapsed with the data of Moser *et al.* (1999).

Thus, despite a potentially different transition mechanism, the statistics behave similarly in cases SLS and T3B, and the changes involved are rather subtle. This observation underlines the value of detailed flow visualizations to supplement statistical quantities.

A.4. Transition in the SLS cases

In this section we provide additional details on the transition in the SLS case. Two-dimensional slices parallel to the wall, shown in figure 25, track the development of the streak that was shown in figure 18a. The first column, a – e, shows contours of the streamwise velocity fluctuation in an xz-plane, and the second column, b – f, contours of the wall-normal velocity fluctuation. In this, as in all similar figures, the plane is located in the lower regions of the transitional boundary layer. Time is normalized with $T = R/U_\infty$.

The breakdown as an asymmetric streak wiggle at $(x, y) = (104, 14)$, $t = 136$ (figure 25a–b). No definite symmetry or asymmetry, however, could be detected in the spot itself. This is most likely due to a higher level of background turbulence than present in the simulations of Brandt *et al.* (2004). The natural spreading rate of this spot is difficult to estimate because of the limiting size of the simulation box. At $x = 142$, $t = 211$ (figure 25e–f), fifty units downstream of the initial instability, the spot occupies two thirds of the spanwise domain.

In figure 26 we track the development of the streak shown in figure 18b into a turbulent spot. The instability originates as a wiggle in a low-speed streak at position $(x, y) = (77, 13)$, $t = 238$ (figure 26a–b), and displays prominent lateral (*i.e.* spanwise) symmetry in the u- and v-velocity components up to $x \simeq 127, t = 313$ (figure 26e–f). The w-component is antisymmetric (not shown). Its development farther downstream is disorderly,

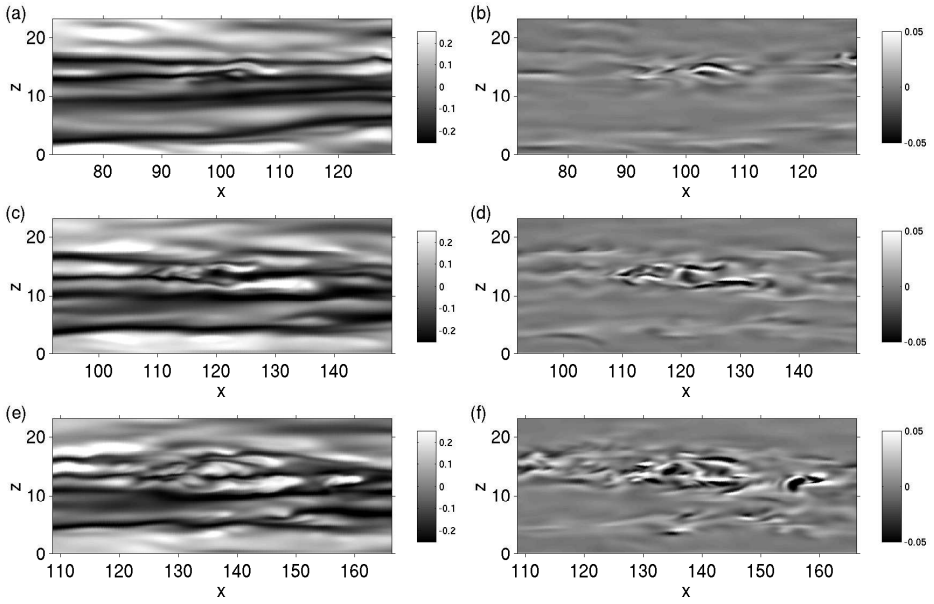

Figure 25: Contours of the velocity fluctuations for a turbulent spot of the first type (see figures 18a,b). Case SLSs; $y = 0.4$; a), c), e) streamwise velocity fluctuation; b), d), f) wall-normal velocity fluctuation; a), b) $t = 136$; c), d) $t = 186$; e), f) $t = 211$.

and by $x = 180$, $t = 391$ (figure 26g,h), it has merged with the turbulent front. In its overall appearance, this spot is similar to the ones shown by Jacobs & Durbin (2001) and Brandt *et al.* (2004) in figures 9 and 11 of these references, respectively.

A qualitative comparison of SLSs/f flow fields is made in figure 28, which shows instantaneous contours of the streamwise velocity fluctuation in the xz-plane inside the boundary layer. Higher-amplitude near-wall disturbance environment near the leading edge is seen for case SLSf, and the corresponding boundary layer appears more disturbed throughout the domain, consistent with the more rapid transition. Aside from the differences in the overall perturbation levels, the two flow fields are very similar. This suggests that the underlying transition mechanism is the same in both instances and appears to be accompanied by Klebanoff modes.

A.5. Turbulent spots in the T3Bf case

Figures 29a,b correspond to a young turbulent spot from the T3Bf simulation, and should be compared with figures 16e,f, respectively, which show a turbulent spot in a similar stage of development for case T3Bs.

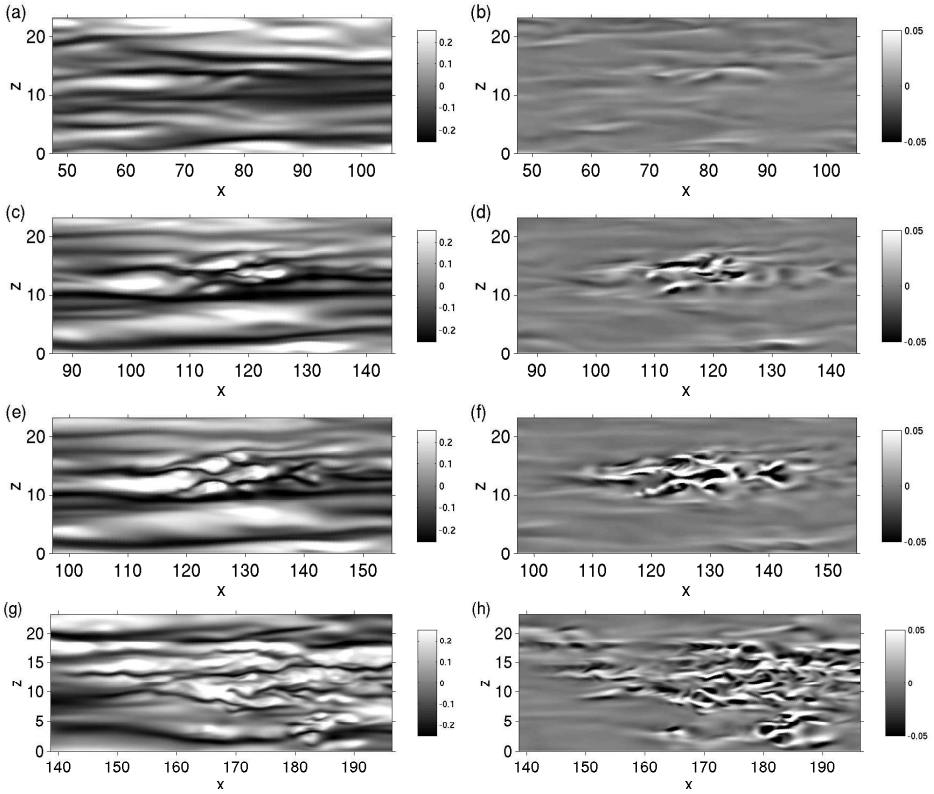

Figure 26: Contours of the velocity fluctuations for a turbulent spot of the second type. Case SLSs; $y = 0.4$; a), c), e), g) streamwise velocity fluctuation; b), d), f), h) wall-normal velocity fluctuation; a), b) $t = 238$; c), d) $t = 296$; e), f) $t = 313$; g), h) $t = 391$.

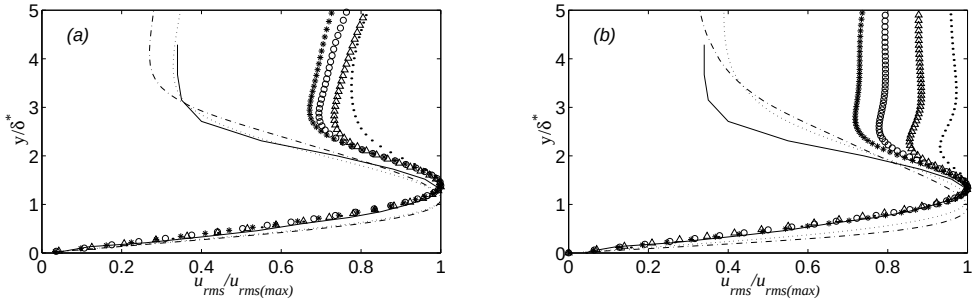

Figure 27: Normalized profiles of u_{rms} across the boundary layer; δ^* is the local displacement thickness; a) Case SLSs; b) Case SLSf; $\bullet$ $x = 4$, $\triangle$ $x = 8$, $\circ$ $x = 12$, $*$ $x = 15$, ····· $x = 54$, —·— $x = 73$; —— self-similar profiles from wind tunnel measurements of Matsubara & Alfredsson (2001);

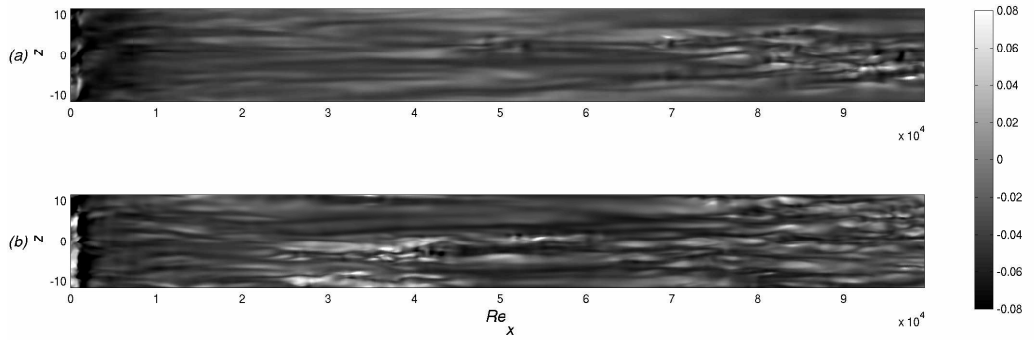

Figure 28: Contours of the streamwise velocity fluctuation inside the boundary layer; (a) Case SLSs; (b) Case SLSf; $y = 0.04$.

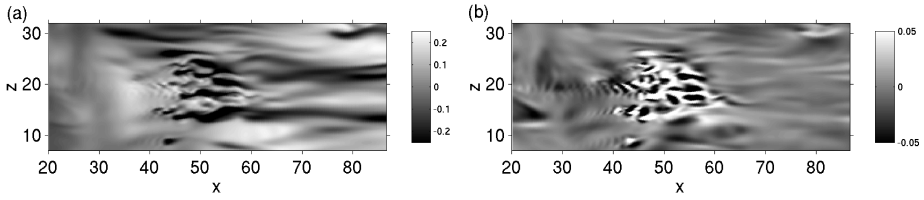

Figure 29: Contours of velocity fluctuations for a turbulent spot of the first type. Case T3Bf; $y = 0.68$; a) streamwise velocity fluctuation; b) wall-normal velocity fluctuation.

A.6. Instability of horseshoe vortices

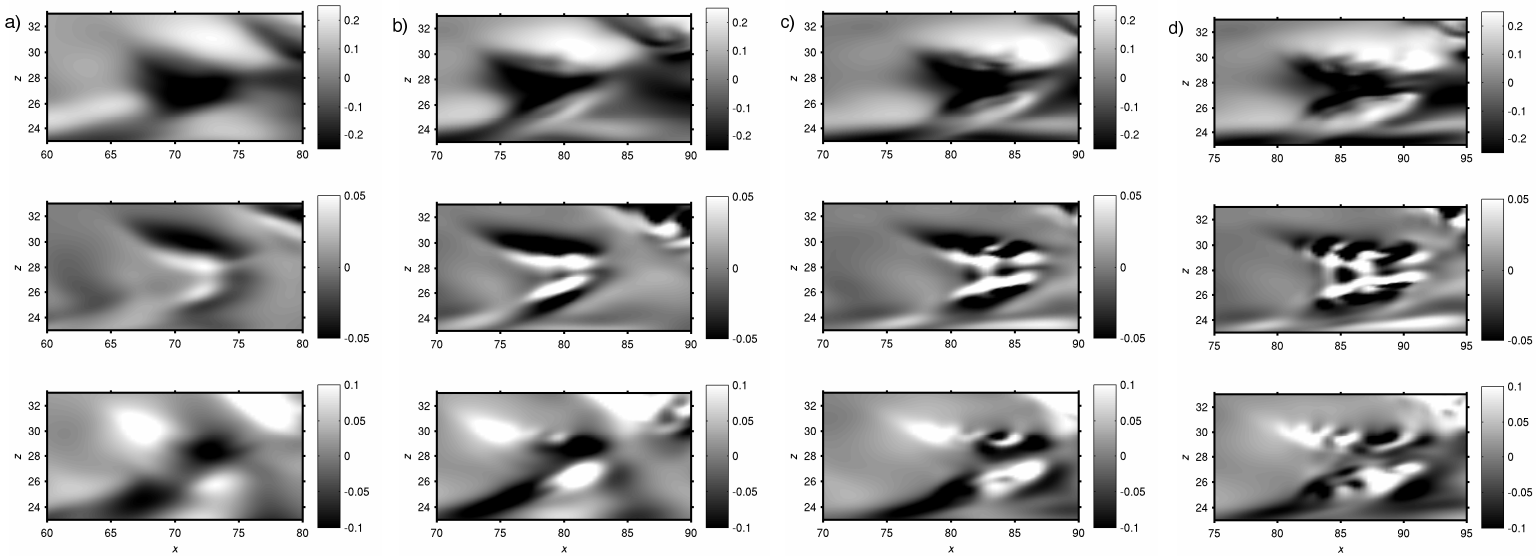

Figure 30: Contours of velocity fluctuations illustrating the breakdown of a horseshoe vortex in the T3Bs simulation; y=0.68. Top: streamwise velocity fluctuation, u'; middle: wall-normal velocity fluctuation, v'; bottom: spanwise velocity fluctuation, w'; a) t=295, b) t=309, c) t=315, d) t=322.

Figure 30 shows a magnified view of a horseshoe vortex undergoing breakdown to turbulence. This vortex is visible in figure 17f, at $(x, z) = (80, 28)$. Oscillations in the wall-normal fluctuation velocity, v', are the most pronounced feature of the breakdown.

REFERENCES

Brandt, L., Schlatter, P. & Henningson, D. S. 2004 Transition in boundary layers subject to free-stream turbulence. *J. Fluid Mech.* **517**, 167–198.

Jacobs, G. J. & Durbin, P. A. 2001 Simulations of bypass transition. *J. Fluid Mech.* **428**, 185–212.

Matsubara, M. & Alfredsson, H. 2001 Disturbance growth in boundary layers subjected to free-stream turbulence. *J. Fluid. Mech.* **430**, 149–168.

Moser, R. D., Kim, J. & Mansour, N. N. 1999 Direct numerical simulation of turbulent channel flow up to $Re_\tau = 500$. *Phys. Fluids* **11**, 943–945.

Roach, P. E. 1987 The generation of nearly isotropic turbulence by means of grids. *Intl J. Heat Fluid Flow* **8** 82–92.